Stable attitude deorbiting using a simplified planar quasi-rhombic-pyramid sail

Narcís Miguel[a,*], Camilla Colombo[a]

[a]*Department of Aerospace Science and Technology, Politecnico di Milano, Milan, Italy*

Abstract

The use of solar sails as passive deorbiting devices has been studied and justified as an effective strategy in the recent literature. There are different possibilities on how to use solar sails to that end, and these can be classified based on how is the attitude of the spacecraft controlled. The proposed strategies consist either of maximising the solar radiation pressure acceleration during the whole trajectory or of switching from maximal to minimal effect along the orbit according to different approaches which requires a different solar sail attitude control.

This paper addresses the possibility of effectively and passively deorbiting spacecraft using an analogue to the quasi-rhombic-pyramid concept to planar motion with the ultimate goal of suppressing the need of attitude control by achieving passive attitude stabilisation. Special attention is paid to the transition from solar radiation pressure to drag dominated regions.

Keywords: Solar sails, end-of-life, solar radiation pressure, atmospheric drag, autostabilisation

Nomenclature

P	Panel
w, h	Width and height of panel [m]
α	Aperture angle [deg or rad]
d	Centre of mass - centre of pressure offset [m]
m_s, m_b	Mass of sail structure and bus [kg]
s_b	Bus side length [m]
C	Inertia moment along rotation axis [kg m^2]
ζ	Rotation axis
φ	Euler angle [deg or rad]
ϕ	Relative orientation [deg or rad]
M	Torque along rotation axis [kg m^2 s^{-2}]
$\mathbf{F}$	Force vector [kg m s^{-2}]
$\mathbf{u}$	Unitary vector
$\mathbf{n}$	Unitary normal vector
p_{SR}	Solar radiation pressure at 1 AU [N/m^2]
A_{exp}	Area exposed to sunlight or atmosphere [m^2]
η	Reflectance of the panels
ρ	Atmospheric density [kg/m^3]
C_D	Drag coefficient
x, y, z	Earth centered inertial frame coordinates
$R_\oplus$	Mean radius of the Earth [km]
$\mu_\oplus$	Mass parameter of the Earth [km^3/s^2]
J_2	Coefficient of the second zonal harmonic

Subscripts

$_{x,y,z}$	Along the direction x, y, z
$_\pm$	Referred to panel $P_\pm$
$_{\mathrm{SRP}}$	Referred to solar radiation pressure
$_{\mathrm{drag}}$	Referred to atmospheric drag
$_{\mathrm{S}}$	Referred to Earth-Sun vector
$_{\mathrm{rel}}$	Referred to the relative velocity vector
$_{\mathrm{GG}}$	Referred to gravity gradient

*Corresponding author, narcis.miguel@polimi.it

1. Introduction

The growing population of space debris in the last decades has increased the interest and need for end-of-life disposal devices and strategies. Recent literature has focused on the idea of carrying an on-board deployable surface that increases the area-to-mass ratio of spacecraft to enhance either the effects of Solar Radiation Pressure (SRP) or the effects of atmospheric drag [1, 2, 3, 4]. The enhancements of SRP acceleration for deorbiting apply for high altitude orbits, whereas atmospheric drag is useful for lower altitudes, but in either case the maximisation of their effect on the orbit for any purpose requires attitude control.

Concerning the SRP, in [5] different strategies were compared: on the one hand, the so-called *passive* approach [2] that consists of maximising the cross area exposed to the sunlight direction to increase the eccentricity of the orbit on the long term an hence to reduce the perigee radius; and on the other hand the so-called *active* strategy that consists of maximising the cross area when travelling towards the Sun and minimising it when travelling away from it to reduce the semi-major axis of the orbit [6]. An approach derived from the latter, called *modulating* and introduced within the ReDSHIFT Project [5] consists of exploiting the SRP enhancements when secular and long-term evolution of the eccentricity is positive, was also put to the test. The passive strategy was found to be the most effective technique for short deorbiting times, while active approaches were of interest for longer deorbiting times.

The main drawback of these approaches is that attitude control is required. In [7] the idea of the usage of a Quasi-Rhombic Pyramid (QRP) shape for the sail was used. Such shape is meant to cancel the components of acceleration that are not along the sunlight direction, in average. These structures and variations of it have been studied in the recent literature, with studies that range from dynamics of these kind of structures to applications, see, e.g. [8, 9, 10, 11, 12, 13].

The goal of this paper is to study the dynamics and performance for deorbiting purposes of these kind of sails in transitions from orbits in SRP dominated regions to atmospheric drag dominated regions, where one expects to see auto-stability properties either around velocity relative to the atmosphere (due to drag) or around the direction of sunlight (due to SRP). To this end, a simplification of the original QRP that avoids out-of-plane motion is considered. In [13] the effects of SRP and drag were studied separately for these family of sails, showing that one can find stable attitude dynamics far from sunlight or velocity vector; namely there seems to be a non-negligible region of stable oscillations in both cases. Here the interaction between the two effects is studied.

The paper is organised as follows. First, in § 2 the family of sails under consideration are described, together with the main physical parameters they depend on. In § 3 the models of the attitude and orbit evolution are provided, together with a list of remarks on attitude dynamics, dynamics on the SRP dominated regions and on autostabilisation of the family of sails considered. In § 4 the main numerical experiments is justified in light of the previous remarks and the available literature, and the main numerical results on autostabilisation are shown and explained. The contribution finishes in § 5 with conclusions and future lines of research that emerge from this paper.

2. Geometry of the sail structure

The class of spacecraft considered here consist of a payload attached to an already deployed deorbiting device. This device is a sail that consists of two equal rectangular panels of width and length w, h, respectively, attached to one of each h-long side, see Fig. 1. This is a simplification of the QRP that avoids out-of-plane motion, that is considered to happen on the ecliptic plane. The payload is assumed to be on a principal axis of inertia as depicted in Fig. 2. The rotations can only occur around an axis that is perpendicular to the normal vectors of both panels, call it ζ, that is in fact a principal axis of intertia of the body frame $\mathcal{F}_b$.

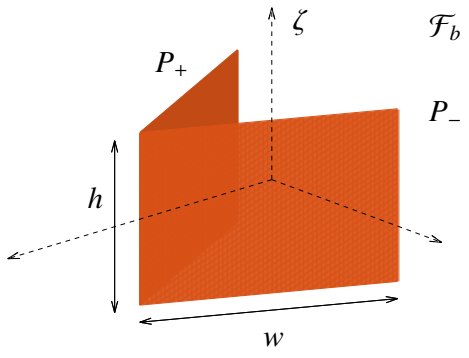

Figure 1: Sketch of the sail structure, 3D view.

Apart from the size, mass and reflectance (physical) parameters, that characterise the area-to-mass ratio and

the size of the acceleration perturbation due to either SRP or drag, the main physical descriptive parameters of the structures are

- The aperture angle $\alpha \in (0, \pi/2)$ rad, defined as the angle formed by the each panel with respect to the axis where the payload is assumed to be on, and
- The center of mass - center of pressure offset d, measured in meters, defined as the (signed) distance between the center of mass of the payload and the sail structure.

These two parameters α and d are depicted in the sketch of the top view of Fig. 1 in Fig. 2, where the sail panels appear as the red (grey) segments and the payload is represented by the black dot.

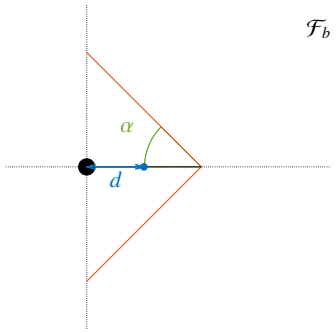

Figure 2: Top view of the spacecraft. The bus is depicted as a black solid circle. Here $d < 0$.

If m_s, m_b denote the mass of the whole sail structure and bus, respectively, the bus is cubic with side s_b, after putting the center of mass of the whole spacecraft at the origin of the body frame $\mathcal{F}_b$, the inertia moment along the ζ axis can be written as

$$C = \frac{1}{6} m_b s_b^2 + D, \text{ where} \tag{1a}$$

$$D = \frac{1}{6} m_s w^2 \cos^2\alpha + \frac{d^2 m_b^2 (m_b + 2m_s)}{(m_b + m_s)^2}. \tag{1b}$$

3. Model

The model used in this paper is a coupled system of translational and rotational differential equations. These were derived in [13], and the reader is referred to this reference for further details. The orbit dynamics is the J_2 problem - the motion of a massless particle around an oblate planet keeping only the second degree zonal harmonic of the expression of the perturbing potential - perturbed by SRP and atmospheric drag forces, written in an Earth center inertial frame $\mathcal{F}_I$. Denote the variables x, y, z, and $\mathbf{i}_x, \mathbf{i}_y, \mathbf{i}_z$ the vectors of the basis. As the problem is planar, the vector $\mathbf{i}_z$ is parallel to the rotation axis of the spacecraft and perpendicular to the orbital plane. This is coupled with the attitude dynamics, whose equations of motion can be written as only depending on one single Euler angle $\varphi \in [0, 2\pi)$ rad that describes the orientation of the body frame $\mathcal{F}_b$ with respect to $\mathcal{F}_I$, as

$$C\ddot{\varphi} = M, \tag{2}$$

where M is the sum of the torques under consideration, and C is the inertia moment along the ζ axis defined in Eq. 1.

It is important to note that the spacecraft shadows itself, fact that has to be taken into account when writing the expressions for torques and accelerations. Let λ denote the angle defined by the position of the Sun with respect to $\mathbf{i}_x$; and let δ be the flight path angle, see Fig. 3. The torques and accelerations due to SRP and drag depend on the value of $\varphi - \lambda$ and $\varphi - \delta$, respectively, through the direction in which each force acts and on the exposed area of the panels. The expressions in both cases are analogous, but the role played by λ in SRP is played by δ in drag. To simplify the notation, and to stress the analogy between the two effects, let us here use the same symbol ϕ to denote the relative orientations, either $\varphi - \lambda$ for SRP or $\varphi - \delta$ for drag.

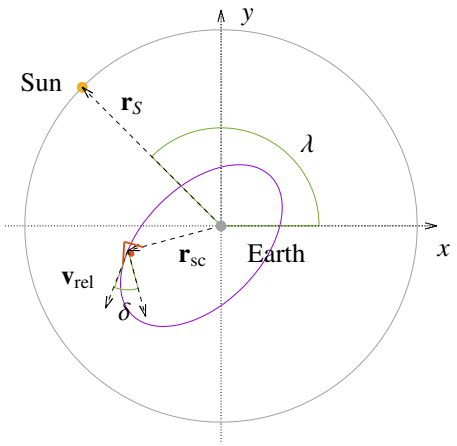

Figure 3: Sketch of the main elements that play a role in the dynamics of the studied family of spacecraft in the Earth centered inertial frame $\mathcal{F}_I$.

Table 1 is a summary of the area A_{exp} that is exposed to either the SRP or the drag flux for each possible relative orientation.

It is straightforward to see that the width of the panel that is not self-shadowed (see the cases $\phi \in (-\pi +$

$\phi = \begin{cases} \varphi - \lambda, \text{ or} \\ \varphi - \delta \end{cases}$	Exposed area A_{exp}	
	P_+	P_-
$[-\pi, -\pi + \alpha]$	$h \cdot w$	$h \cdot w$
$(-\pi + \alpha, -\pi/2]$	$h \cdot w$	$h \cdot w'(-\phi)$
$(-\pi/2, -\alpha]$	$h \cdot w$	0
$[-\alpha, \alpha]$	$h \cdot w$	$h \cdot w$
$(\alpha, \pi/2)$	0	$h \cdot w$
$[\pi/2, \pi - \alpha)$	$h \cdot w'(\phi)$	$h \cdot w$
$[\pi - \alpha, \pi)$	$h \cdot w$	$h \cdot w$

Table 1: Exposed area as a function of the relative orientations.

$\alpha, -\pi/2]$ and $\phi \in [\pi/2, \pi - \alpha)$ in Tab. 1) can be written as

$$w'(\phi) = 2w\frac{\cos\phi \sin\alpha}{\sin(\alpha - \phi)}.$$

Remark that the accelerations and torques due to SRP and atmospheric drag are piecewise smooth, and they have $\phi = \pm\pi \mp \alpha$, $\phi = \pm\pi/2$ and $\phi = \pm\alpha$ as switching manifolds, where the equations lose differentiability with respect to ϕ, but not continuity.

3.1. Force models

The acceleration due to SRP and atmospheric drag are considered. Following [14], the force due to SRP exerted to the panel $P_\pm$ whose exposed area is A_{exp} is

$$\mathbf{F}^{\pm}_{\text{SRP}} = -p_{\text{SR}} A_{\text{exp}} (\mathbf{n}_\pm \cdot \mathbf{u}_{\text{S}}) \, (2\eta(\mathbf{n}_\pm \cdot \mathbf{u}_{\text{S}})\mathbf{n}_\pm + (1 - \eta)\mathbf{u}_{\text{S}}), \quad (3)$$

where $\mathbf{n}_\pm$ are the normal vectors to the sail panels, $\mathbf{u}_{\text{S}}$ is the direction of the Earth-Sun vector, see Fig. 3, $\eta \in (0, 1)$ is the (dimensionless) reflectance[1] of the sail and $p_{\text{SR}} = 4.56 \times 10^{-6}$ N/m^2 is the solar pressure at 1 AU, that is considered to be constant.

Concerning atmospheric drag, the force exerted to panel $P_\pm$ reads

$$\mathbf{F}^{\pm}_{\text{drag}} = -\frac{1}{2}\rho v_{\text{rel}}^2 C_D A_{\text{exp}} (\mathbf{n}_\pm \cdot \mathbf{u}_{\text{rel}}) \mathbf{u}_{\text{rel}}, \quad (4)$$

where $\mathbf{u}_{\text{rel}}$ is the direction of relative velocity vector, v_{rel} is its modulus, so $\mathbf{v}_{\text{rel}} = v_{\text{rel}}\mathbf{u}_{\text{rel}}$, see Fig. 3, ρ is the atmospheric density in kg/m^3, and $C_D \in (1.5, 2.5)$ is an empirically determined dimensionless drag coefficient. For simulations, the model used to retrieve the of atmospheric density is that proposed in [15].

[1] In the literature the notation $c_R = 1 + \eta$ is used, and it is referred to as reflectivity coefficient.

3.2. Orbit dynamics

Building on previous contributions on the usage of SRP to design end-of-life disposals, see [2, 1, 4, 5], the J_2 problem perturbed by SRP and atmospheric drag forces is considered. Here the effect of eclipses is not taken into account. In Cartesian coordinates, the equations read

$$\ddot{x} = -\frac{\mu_\oplus x}{r^3} - \frac{3R_\oplus^2 \mu_\oplus J_2}{2}\frac{x}{r^5} + a_x + b_x \quad (5a)$$

$$\ddot{y} = -\frac{\mu_\oplus y}{r^3} - \frac{3R_\oplus^2 \mu_\oplus J_2}{2}\frac{y}{r^5} + a_y + b_y, \quad (5b)$$

where $r = \sqrt{x^2 + y^2}$, $\mu_\oplus = 3.986 \times 10^{14}$ m^3/s^2 is the mass parameter of the Earth, $R_\oplus = 6378.1$ km is the mean Earth radius, and a, b refer to the acceleration due to SRP and drag, respectively. These are the sums of the accelerations due to each panel in the corresponding direction factored by the non-shadowed area given in Tab. 1. Note also that $\mathbf{r}_{\text{S}} = r\mathbf{u}_{\text{S}}$, see Fig. 3.

3.3. Attitude dynamics

The attitude dynamics is governed by the set of 2 differential equations given in Eq. 2, where

$$M = M_{\text{SRP}} + M_{\text{drag}} + M_{\text{GG}},$$

each of the summands being the torques due to SRP, drag and Gravity Gradient (GG), respectively. In [13] the authors justified that the torque due to panel $P_\pm$ of SRP is of the form

$$\frac{A_{\text{exp}}}{m_b + m_s}\frac{p_{\text{SR}}}{2} M_0^{\pm}(\varphi - \lambda, \eta), \quad (6)$$

where

$$M_0^{\pm}(\psi, \eta) = -\frac{1}{2}k_{1,1}(\eta)\sin(2\psi) \pm k_{2,0}(\eta)\cos^2\psi \pm k_{0,2}(\eta)\sin^2\psi \quad (7)$$

and

$$k_{1,1}(\eta) = \sin\alpha[2dm_b(2\eta\cos(2\alpha) + \eta + 1) + w(m_b + m_s)(\cos\alpha - \eta\cos(3\alpha))], \quad (8a)$$

$$k_{2,0}(\eta) = \sin^2\alpha[4d\eta m_b \cos\alpha + w(m_b + m_s)(1 - \eta\cos(2\alpha))], \text{ and} \quad (8b)$$

$$k_{0,2}(\eta) = \cos\alpha[2dm_b(\eta\cos(2\alpha) + 1) + \eta w(m_b + m_s)\sin\alpha\sin(2\alpha)]. \quad (8c)$$

The advantage of this formulation is that the torque due to panel $P_\pm$ due to atmospheric drag force can be

written using the functions $M_0^{\pm}$, $k_{1,1}$, $k_{2,0}$ and $k_{0,2}$ but with $\eta = 0$; namely it reads

$$\frac{A_{\exp}}{m_b + m_s} \frac{\rho v_{\rm rel}^2 C_D}{4} M_0^{\pm}(\varphi - \delta, 0). \tag{9}$$

Note that the dependence on the relative orientation of $A_{\exp}$ is reflected in the expressions given in Tab. 1.

Finally, concerning the torque due to the gravity gradient, since the bus is assumed to be symmetric, it reads

$$-\frac{3\mu_\oplus}{2r^3} \frac{D}{C} \sin(2(\arctan(y/x) - \varphi)), \tag{10}$$

recall Eq 1.

3.3.1. Some remarks on attitude dynamics

The main purpose of this paper is the exploration of the possibilities of structures such as those sketched in Fig. 1 in transitions from SRP dominated regions to drag dominated regions for their auto-stabilising properties. In either SRP or drag dominated region, the attitude dynamics is expected to be of the form

$$C\ddot{\varphi} \quad = \quad M_\star + \text{ other effects},$$

where $\star$ is either SRP or drag, and the other two remaining effects (drag or SRP, depending of what $\star$ refers to, and gravity gradient) are expected to be smaller. This suggests to study the system

$$\psi'' \quad = \quad M_{\rm SRP}, \tag{11}$$

where $(') = \mathrm{d}/\mathrm{d}s$ and s is a time variable (obtained by a constant scaling of the original time variable t) chosen so that one gets rid of the prefactor of Eq. 6 and of C; and $\psi = \varphi - \lambda$ consists of shifting the sun-pointing direction to the origin. This reduction is justified and performed in full detail in [12]. Here SRP is chosen instead of drag for two reasons: on the one hand, the pressure close to Earth is assumed to be constant, recall § 3.1, so it does not depend on the actual orbit we are on but only on time, and on the other hand, the expression for drag is just the particular case of the SRP problem with $\eta = 0$.

For system Eq. 11 the sun-pointing direction $E_0 : \psi = 0, \psi' = 0$, and its reverse $E_1 : \psi = -\pi, \psi' = 0$ are equilibria. In [12] it was proven that a necessary condition for the stability of E_0 (and hence the instability of E_1 due to the sign change) is that $d > d_{\min}$, where

$$\begin{aligned} d_{\min} &= \frac{w(m_b + m_s)}{2m_b} K(\alpha, \eta), \text{ where} \\ K(\alpha, \eta) &= \frac{\eta\cos(3\alpha) - \cos\alpha}{2\eta\cos(2\alpha) + \eta + 1}. \end{aligned} \tag{12}$$

Note that $d_{\min} < 0$ [13] and this condition has the physical interpretation of being the longest distance between sail structure and payload behind the structure, as depicted in Fig. 2, so that the sun-pointing direction is stable.

The existence of other equilibria depends on the values of the three parameters α, d and η, and has to be numerically tackled. From Eq. 11, the set of equilibria are those points on ψ, ψ' such that $\psi' = 0$ and $M_{\rm SRP}$ vanishes.

To fix ideas, the values $\eta = 0, 0.8$ are used. The latter corresponds to drag while the former is a typical reflectance value. As the parameter η is fixed, the parameter space is 2-dimensional depending on α and d.

Assume that $d > d_{\min}$, that is, the sun-pointing direction E_0 is stable (this case is depicted in the forthcoming Fig. 5). The parameter space can be divided into regions according to the number of equilibria the system has. As $M_{\rm SRP}$ is symmetric, $M_{\rm SRP}(-\psi) = -M_{\rm SRP}(\psi)$ and $E_{0,1}$ are always equilibria there is numerical evidence that there are either 2, 4 or 6 equilibria, as depicted in Fig. 4. A description of each of these 3 cases follows.

(1) Only $E_{0,1}$ are equilibria, E_0 is stable and E_1 is unstable. This is true also in the other two cases. See Fig. 4 top.

(2) The equilibria are $E_{0,1}$ and two other equilibria at $\psi = \pm\psi_{\rm bif}(\alpha, d, \eta)$ at bifurcation, where $M_{\rm SRP}$ is tangent to $\psi' = 0$. See Fig. 4 middle.

(3) The equilibria are $E_{0,1}$ and two pairs of stable-unstable equilibria that bifurcate from the previous bifurcation points. Fig. 4, bottom.

The bifurcation is of the saddle-center type, that is of co-dimension one so it can be locally explained by one single parameter. As η is assumed to be fixed, our system depends on 2 parameters, one expects to be able to find a curve of bifurcations in the (α, d) plane that separates the set of parameters for which there are 2 and 6 equilibria. The bifurcation curve would be the set of parameters for which there are 4 equilibria.

This is the contents of Fig. 5, where on top (resp. bottom) the bifurcation diagram for $\eta = 0$ (resp. $\eta = 0.8$) is displayed. In both panels, the plane is separated in 3 regions: below the red (dashed) line, that represents $d = d_{\min}$, recall Eq. 12. Below this line E_0 is not a stable equilibrium and this set is not relevant for this contribution. The region labelled as "case (3)" between the red (dashed) and blue (solid) curve are the value of the parameter for which Eq. 11 has six equilibria. Above

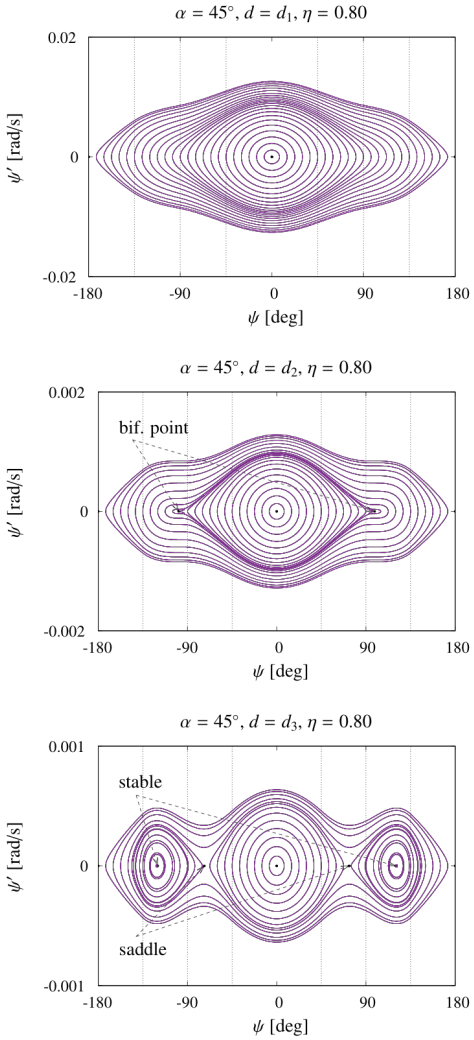

Figure 4: Phase space of Eq. 11 for $\alpha = 45°$, $\eta = 0.8$. The choices of the parameter d is done so that: Top, M_{SRP} vanishes twice in $[-\pi, \pi)$; middle: four times; bottom: six times. The vertical dotted lines indicate the switching manifolds.

the blue (solid) line, in the region labelled as "case (1)", only $E_{0,1}$ are equilibria of Eq. 11. The transition "case (2)" blue (solid) curve is the line of bifurcation points, and the parameter values on this curve are those for which Eq. 11 has exactly 4 equilibria. In the bottom panel of Fig. 5 the values

$$\begin{aligned} d_1 &= 0 \text{ m}, \\ d_2 &= -2.60342454037092 \text{ m, and} \\ d_3 &= -2.98660630839676 \text{ m} \end{aligned}$$

for $\alpha = 45°$ are highlighted. The value d_2 is a numerically approximated bifurcation point. These are the examples in Fig. 4, where the values of d used is indicated in the title of each panel.

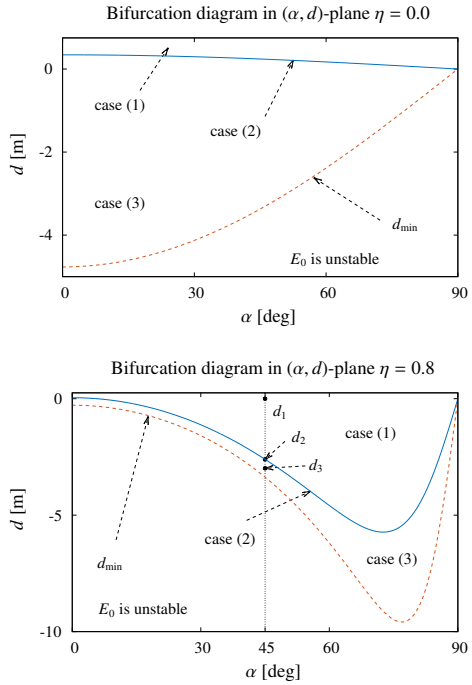

Figure 5: Bifurcation diagrams in the (α, d) parameter space. Top: $\eta = 0.0$. Bottom: $\eta = 0.8$. The blue (solid) line is the bifurcation curve, while the red (dashed) line is d_{min}, see Eq. 12.

These remarks should be taken into account when designing any control strategies that include the change of aperture angle α. In the examples shown in Fig. 4 even though the bifurcation occur inside the main region of stability it may happen, as is typical in conservative systems, that as parameters change, the stability region can separate in more than one connected component and hence the overall global dynamics would drastically change, see [16].

Note that this numerical study can also be performed considering the parameter η. This can be of interest for control strategies based on electrochromic properties of the sail panels, see [3].

3.3.2. Some remarks on SRP dominated regions

If the motion starts above 800 km of altitude the atmospheric drag effect is negligible and the problem reduces to SRP perturbed J_2 problem for orbit dynamics and the attitude dynamics is that of SRP and gravity gradient, that can be interpreted as a perturbation of the latter, see [13]. The coupled attitude and orbit dynamics in this regime can be reduced to a fairly simple problem after first separating the rotational and translational

dynamics and then using single averaged theory. Summarising, one would proceed as follows

1. The separation of attitude and orbit dynamics was formally addressed in [12]. The main result is that if the sail is initially oriented towards sunlight in a way that both panels face it, namely $|\varphi - \lambda| < \alpha$, recall Tab. 1, for large enough area-to-mass ratio, the oscillating motion around the Earth-Sun vector can be averaged out. This procedure leads to a system that consists only of the orbital equations of motion, perturbed by a term that can interpreted as the SRP effect of a flat sail always perpendicular to the Earth-Sun vector along the motion. The area of this 'equivalent' sail depends on the area of the panels of the original structure (Fig. 1), the aperture angle α, the reflectance η and the initial amplitude of the oscillations around the Earth-Sun vector. An explicit formula was also provided. If one assumes that the sail is initially pointing exactly in the direction of the Earth-Sun vector $\varphi = \lambda$, i.e., the amplitude of the oscillations with respect to the Sun is initially 0, the *effective* area of the sail is
$$A_{\text{eff}} \quad = \quad h \cdot w \cdot \left[(2+\eta)\sin\alpha - \eta\sin(3\alpha)\right]. \quad (13)$$
2. After the previous reduction the problem to deal with is the two-body dynamics of a spacecraft with high area-to-mass ratio perturbed by J_2 effect and SRP. This can be further simplified via single averaging [17, 18, 19]. In the proposed formulation, the semi-major axis a is constant in average, and the averaged variation of the eccentricity e and $\beta = \omega - \lambda + \pi$, where ω is the longitude of the pericenter of the osculating orbit, can be written in Hamiltonian form with Hamiltonian function
$$H \; = \; -\sqrt{1-e^2} + W_1 e\cos\beta - \frac{W_2}{3(1-e^2)^{3/2}}, \quad (14)$$
where W_1 and W_2 are constants related to SRP and J_2 effects, respectively, that read
$$W_1 \quad = \quad \frac{3}{2}p_{\text{SR}}(1+\eta)\frac{A_{\text{eff}}}{m_b+m_s}\frac{a^2}{\mu_\oplus}\frac{n}{n_\odot} \quad (15a)$$
$$W_2 \quad = \quad \frac{3}{2}J_2\frac{R_\oplus}{a^2}\frac{n}{n_\odot}, \quad (15b)$$
where $n = 2\pi\sqrt{\mu_\oplus/a^3}$ and $n_\odot$ are the mean motion on the orbit and of the apparent motion of the Sun, respectively.
This formulation was exploited in [1, 2] as the theoretical framework of the so-called passive deorbiting strategy. Recall that, as mentioned in the introduction, these papers dealt with finding the area-to-mass requirements so that the dynamics lead to an increase of the eccentricity of the orbit as this, in turn, causes a decrease the perigee radius. See also [20] for a description of the phase space of this problem.

3.3.3. Some remarks on attitude stability

The stability of a solar sail structure as that sketched in Fig. 1 was studied in [13], where numerical evidence of the existence of attitude-stable orbits was provided. In this cited reference the considered the equations of motion were the orbit ones as in Eq. 5 coupled with attitude taking into account either SRP+GG or drag+GG effects, studied separately to focus on attitude initial conditions that remained close the sun-pointing direction or the relative velocity vector, respectively.

The main results are evidence of the existence of a set of effective stability (meaning that the stability property is conserved for long time spans but there is not yet any rigorous justification of this fact) close to the corresponding directions of interest. On the other hand, the numerical results in [13] for the drag+GG case justify that deorbiting can be achieved along an orbit where the attitude is maintained by itself via autostabilisation close to the relative velocity vector.

4. Numerical study

The remarks of the previous section give a global perspective on the possible motions one could be interested in, when trying to deorbit a solar sail as such in Fig. 1, trying to choose initial conditions so that the motion remained stable either close to the sun-pointing direction or close to the relative velocity vector for as much time as possible, without any aid of attitude control.

4.1. Choice of initial conditions and physical parameters

The problem addressed depends on many physical parameters, and the phase space is 6 dimensional -and so is the set of initial conditions to be chosen- so tackling the problem requires reducing the orbits and spacecraft to be studied to the most relevant for the purpose of this paper. Here the remarks done in § 3.3.1, 3.3.2 and 3.3.3 are put together to that end.

Let us first deal with the set of attitude and orbit initial conditions for the simulations. The spacecraft-sun distance is considered to be constant -recall p_{SR} is assumed to be constant-, hence the most reasonable scenario where to find attitude stable orbits in transitions from SRP to drag dominated regions would be among orbits initially on an SRP dominated region, say with

semi-major axes $a \geq R_\oplus + 1000$ km initially pointing close to the Earth-Sun vector. When entering a region where atmospheric drag plays a relevant role, one expects that, as it is a dissipative effect, the spacecraft will naturally deorbit, but as it gets closer to Earth's surface, the drag effect becomes stronger and is hence more likely to destroy the stable attitude character towards sunlight.

Taking this into account, the spacecraft is assumed to be initially placed at an orbit with semi-major axis $a = R_\oplus + 1000$ km, where the drag effect is negligible in front of the SRP effect, pointing exactly towards sunlight, that is, initially $\varphi = \lambda$. Even if the amplitude of the oscillations increase they will do in regions like those depicted in § 3.3.1, so the stable character is less likely to be lost. As exposed in § 3.3.2, the motion in the very beginning of the evolution behaves as if it was a sail of area A_{eff} as given in Eq. 13 always pointing towards sunlight; the semi-major axis remains close to constant in average and the two main orbital elements that characterise most of orbital initial conditions are ω (through β, the argument of the perigee measured with respect to λ) and e.

Despite the Hamiltonian H, see Eq. 14, is symmetric with respect to β, ω is discretised in the whole interval $[0°, 360°)$ as the joint effect of drag, SRP and GG is likely to destroy any symmetry, although some reminiscence of it might still be observed in simulations.

Concerning the choice of the range of e, to have a global point of view of the joint effect of SRP and drag with different initial magnitudes of the drag effect, one should choose values as follows: if the motion starts at an orbit with $a = R_\oplus + 1000$ km, the range of eccentricities to be dealt with should be those that $[0, e_{\text{crit}}]$, where

$$\begin{aligned} R_\oplus + 120 &= (1 - e_{\text{crit}})(R_\oplus + 1000), \text{ that is,} \\ e_{\max} &\approx 0.119, \end{aligned}$$

that is, orbits initially with $a = R_\oplus + 1000$ km, from circular to those whose perigee radius r_p is $R_\oplus + 120$ km, above of what is considered here to be deorbited. The quantity e_{crit} is referred to as the *critical* value of the eccentricity in the literature, see e.g. [1, 2].

Concerning the choice of shape parameters, the value $d = 0$ m has been set, as this parameter was shown not to affect the deorbiting time in the drag+GG problem in [13]. On the other hand the aperture angle has been chosen to be fixed $\alpha = 45°$. In the last cited reference the authors showed evidence that for a fixed panel size, the larger α the smaller the deorbiting time, provided one started at the same altitude with the same relative initial oscillation amplitude. But still, for different aperture angles the deorbiting times are comparable so no qualitative difference is expected to be seen if other values of α are chosen. Furthermore, these choices are justified as the orbit and attitude coupled system can always be scaled in such a way that the attitude dynamics has the same representation [12]. It is important to note that the relevance of d is that it governs the size of the gravity gradient summand Eq. 10 through D, that is proportional to d^2, see Eq. 1b; hence it controls the relative size between the SRP and drag with GG terms. The closer d is to zero, the smaller M_{GG} is and hence the perturbation appearing in the attitude dynamics is smaller.

From the point of view of the orbit dynamics, the size of the SRP and drag accelerations is proportional to the area-to-mass ratio, call it σ. For the same value of a, different values of σ give rise to different phase space configurations of Eq. 14. To exemplify the dependence of the deorbit time and on the attitude stable orbits on σ three different values of σ of the panels $P_\pm$ have been considered for simulations: $\sigma_{1,2,3} = 1, 2, 5$ m^2/kg. The averaged dynamics of sails as in Fig. 1 is that of a sun-pointing flat panel with effective area given by Eq. 13 so at the beginning of the motion the considered sails have an effective area-to-mass ratio that shall be denoted as σ_{eff}. For the three chosen values, they are, approximately,

$$\sigma_1 = 1 \text{ m}^2/\text{kg} \quad \rightarrow \quad \sigma_{1,\text{eff}} = 1.41421356 \text{ m}^2/\text{kg}, \quad (16a)$$
$$\sigma_2 = 2 \text{ m}^2/\text{kg} \quad \rightarrow \quad \sigma_{2,\text{eff}} = 2.82842712 \text{ m}^2/\text{kg}, \quad (16b)$$
$$\sigma_3 = 5 \text{ m}^2/\text{kg} \quad \rightarrow \quad \sigma_{3,\text{eff}} = 7.07106781 \text{ m}^2/\text{kg}. \quad (16c)$$

In Fig. 6 the phase space of H, Eq. 14, for the three values of σ_{eff} considered is shown. The displayed part of the phase space is $\beta \in [0, 360)$ and $e \in [0, 0.12]$, that is, restricted to the zone of interest of the forthcoming computations. The panel in Fig. 6 show the averaged evolution of β and e as a function of time in the very beginning of the simulations. Note that only orbits starting with e close to e_{crit} go beyond e_{crit} so if the spacecraft deorbit atmospheric drag would be the cause for it, that is, deorbiting will be due to a transition to a drag-dominated region.

In summary, the numerical exploration of the problem has been reduced to study deorbiting times and attitude stability along the corresponding orbits starting at the perigee of orbits whose shape and orientation Keplerian elements are $a_0 = R_\oplus + 1000$ km, $e \in [0, 0.119]$ and $\omega \in [0°, 360°)$. The study the behaviour in these ranges has been performed by discretizing among $16 \cdot 16 = 256$ initial conditions in e, ω for each of the 3 values of the

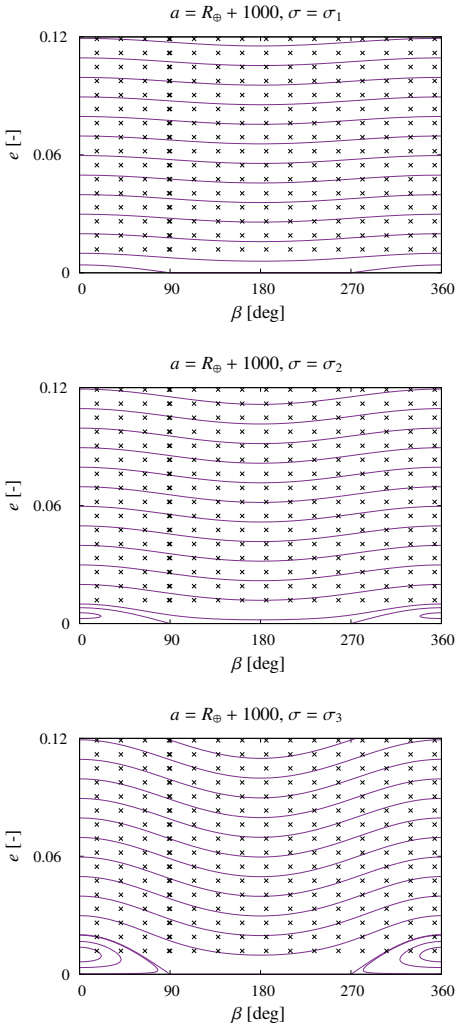

Figure 6: Phase space of H, Eq. 14 for the three values of σ_{eff} in Eq. 16. Purple (solid) lines are contours H = constant, and the black crosses are the initial conditions used in simulations.

area-to-mass ratio, namely

$$a_0 = R_\oplus + 1000 \text{ km}, \quad (17a)$$

$$e_0 = 0.0119(0.0067)0.119 \text{ (16 values), and} \quad (17b)$$

$$\omega_0 = 0°(22.44°)359° \text{ (16 values).} \quad (17c)$$

This discretization is enough for the purposes of this paper as it allows to captures the most relevant qualitative features of the attitude dynamical properties of the sails under consideration. The initial conditions (e and ω) used are crosses in Fig. 6. The attitude has been set initially to $\varphi_0 = \lambda_0 = 90°$, $\dot{\varphi}_0 = 0$ rad/s, that is, exactly towards the sun-pointing direction. The study has been performed for 3 values of $\sigma_{1,2,3}$ of $P_\pm$, 1, 2 and 5 m^2/kg, respectively.

4.2. Results

Each of the $16 \times 16 = 256$ initial conditions in Eq. 17 for each of the three area-to-mass ratios have been integrated from $t = 0$ s until they reached $r = 120$ km. The time span required to reach this state is referred to as the *deorbit time*, let us refer to it as t_{deor}. The goal of this subsection is to describe which is the behaviour from the point of view of attitude of a spacecraft as in Fig. 1 in the interval $[0, t_{\text{deor}}]$.

For convenience, the results are separed into two different parts. First, as spacecraft are initially considered to be pointing towards sunlight, $\varphi = \lambda$, so the contents of § 4.2.1 is to study how long do spacecraft maintain a stable attitude towards the Sun, and what portion of the total deorbiting time is spent in this attitude stable state. The second part of the results, those in § 4.2.2, are focused of what happens after the helio-stable state is lost, until the deorbiting is achieved.

4.2.1. Time spent in a helio-stable state

Along the integration, the amplitude of the oscillations with respect to sunlight, measured simply as $|\varphi - \lambda|$ have been monitored. All initial conditions were chosen as $\varphi = \lambda$, that is, this amplitude was initially zero. In the course of the integration this amplitude changed due to the increasing size of the gravity gradient atmospheric drag torque and drag acceleration. The detection of tumbling attitude dynamics with respect to sunlight, meaning that the rotation is not oscillatory around the sun-pointing direction but librational with respect to it is done by setting a threshold in the maximum amplitude: if a state $|\varphi - \lambda| > 0.9 \times \pi$ rad was reached, the spacecraft was considered to have entered a tumbling mode with respect to the Sun. The second observable of interest here is the time span required to enter this tumbling mode, that is referred to as *helio-stable time*, and is denoted as $t_{\text{h-s}}$. Note that, in particular, $t_{\text{h-s}} \leq t_{\text{deor}}$.

The summary of all numerical results can be seen in Fig. 7 where the deorbit times (left) and helio-stable times (right) are displayed for all considered initial conditions. The top, middle and bottom panels correspond to the area-to-mass ratios σ_1, σ_2 and σ_3, respectively. In each of the plots, data is grouped according to the initial value of e_0: each color (different point style) corresponds to one value of e_0.

Concerning the deorbit times t_{deor}, shown in the left panels of Fig. 7, as expected, that the larger e_0 is, the faster the deorbiting is. Recall that in the absence of the drag effect only the initial conditions whose e_0

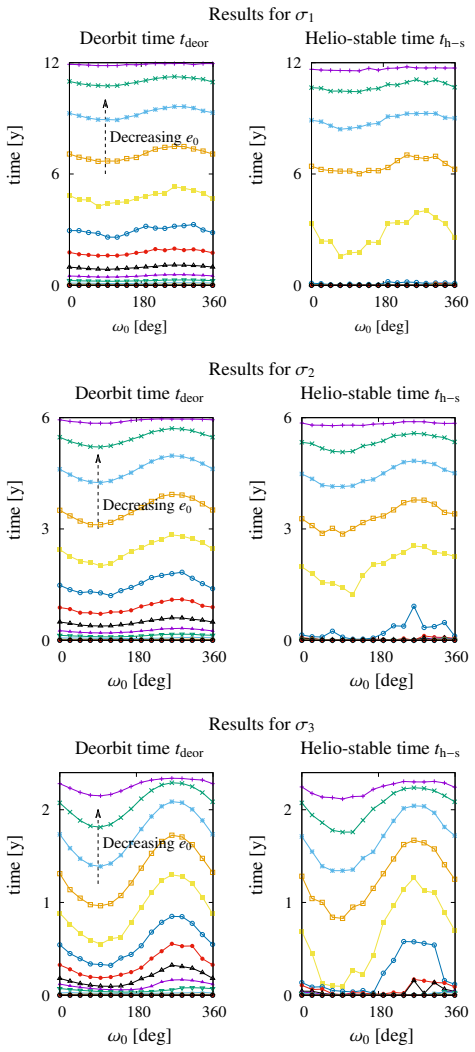

Figure 7: Deorbit times t_{deor} (left column) and helio-stable times t_{h-s}(right column) as a function of the initial ω_0. Points in the same line started in the same e_0. Top to bottom: results for each of the three area-to-mass ratio values considered σ_1, σ_2 and σ_3, respectively.

were close to e_{crit} would have been expected to deorbit. Moreover, roughly, even though there is no theory that supports this numerical evidence, the deorbit times for σ_2 are half the deorbit times for σ_1 and those for σ_3 are one fifth of the deorbit times for σ_1, which is the same arithmetic relation between the area-to-mass ratios, even though the spacecraft oscillate around the sun-pointing direction, that makes the effective exposed are different, according to the oscillation amplitude [12]. Also some reminiscence of the periodicity with respect to ω_0 is visible for smaller values of e_0. It is worth noting that the deorbit times for the maximum value of $e_0 = 0.119$ considered are of the order of magnitude of hours for $\sigma_{1,2}$ and minutes for σ_3.

Concerning the helio-stable times t_{h-s}, shown in the right panels of Fig. 7, the same color code (point style) has been used for the same initial e_0 as in the left plot to allow for comparison. For smaller (uppermost) values of e_0 there seems to be some resemblance but in all cases the inequality $t_{h-s} < t_{deor}$ is satisfied. But for larger values of e_0 the shown scale is not adequate for the visualisation of the differences.

To be able to visualise the differences between t_{deor} and t_{h-s} a relative measure is a more suitable option: for each value of e_0, the fraction of helio-stable time

$$t_{h-s}/t_{deor}$$

has been computed, for all the considered 16 values of ω_0. This defines a curve that has been fitted to a line $f(\omega_0) = c$, where c is a constant, using a least squares procedure[2]. It is worth noting that for some values of e_0 there is a large variation of t_{h-s} for different ω_0. This fit gives measure that allows for comparison between different values of e_0. Each value of c can be interpreted as the averaged percentage of time spent by orbits in a helio-stable state. The results for the three values of σ considered are displayed in Fig. 8.

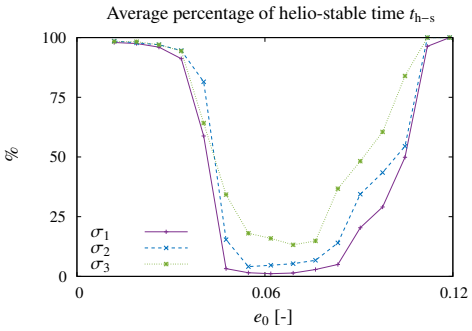

Figure 8: Average time on the orbit spent in a helio-stable state, as a function of the initial eccentricity of the orbit, e_0. In purple (solid line), blue (dashed line) and green (dotted line) the results for σ_1, σ_2 and σ_3 are displayed, respectively.

In Fig. 8 it can be seen that for smaller eccentricities the tumbling state with respect to sunlight starts at the very end of the trajectory, and hence most of the time (above 97% of it for the smallest e_0 for all three σ) is spent in stable oscillation close to the sun-pointing direction. This can be related to the fact that auto-stabilisation of the sail via drag force can be reached for altitudes below 800 km, see [13]. In case the initial

[2]The routine `fit` of `gnuplot` Version 5.2 has been used to this end

value of the perigee radius $r_p < R_\oplus + 800$ km one expects a faster decay as the magnitude of the drag effect is larger.

For larger values of e_0 the results show that most of the time is spent tumbling (or librating with respect to the Sun). The tumbling time decreases back below 10% for eccentricities closer to e_{crit}, where also the deorbiting time is substantially smaller.

4.2.2. Attitude dynamics after the helio-stable state

After leaving a stable oscillation around the sun-pointing direction the motion seems to be librational with respect to sunlight yet the auto-stabilizing shape of the sail structure can lead to drag-stable motion, that is, that the sail starts to oscillate close to the relative velocity vector.

This stability is mostly likely to be reached close the end of the trajectory, right before the spacecraft reaches $= R_\oplus + 120$ km, as the atmospheric density is larger and hence the strength of the drag torques and accelerations are enhanced. In fact, this is actually detected in the orbit data. In order to have a quantitative idea on how much time the spacecraft spends in a drag-stable state, one can proceed as above when detecting the amount of time spent in helio-stable oscillations, but studying the orbit data backwards and monitoring the amplitude with respect to the relative velocity vector, that is, $|\varphi - \delta|$.

Analogously as above, the term *drag-stable time* is used to refer to the instant of time in which the spacecraft enters a drag-stable oscillatory state, and is denoted as $t_{\text{d-s}}$. The way to detect $t_{\text{d-s}}$ is to read the orbit data from the deorbiting time backwards: $t_{\text{d-s}}$ is the instant of time where $|\varphi - \delta| > 0.9\pi$ rad is first reached.

As in § 4.2.1, the numerical results are displayed as a percentage of time spent on a drag-stable state, by averaging

$$t_{\text{d-s}}/t_{\text{deor}}$$

over all values of ω_0, for each value of e_0. The results of the time spent on a drag-stable state are shown in Fig. 9, top. The bottom panel in this same figure is the average time spent neither in a helio-stable nor a drag-stable state, that is, librating with respect to both sunlight and the relative velocity vector. This time span is referred to as *tumbling time* and is denoted as $t_{\text{tumb}} := t_{\text{h-s}} - t_{\text{d-s}}$.

The shown results in Fig. 9 indicate that the drag-stable state is only reached at the very end of the motion. The time spent in this state for the three values of $\sigma_{1,2,3}$ is below 1% for the two smallest values of e_0. Again, for the largest values of e_0 considered, the deorbit time is extremely small compared to the t_{deor} for orbits initially closer to circular, this being the reason

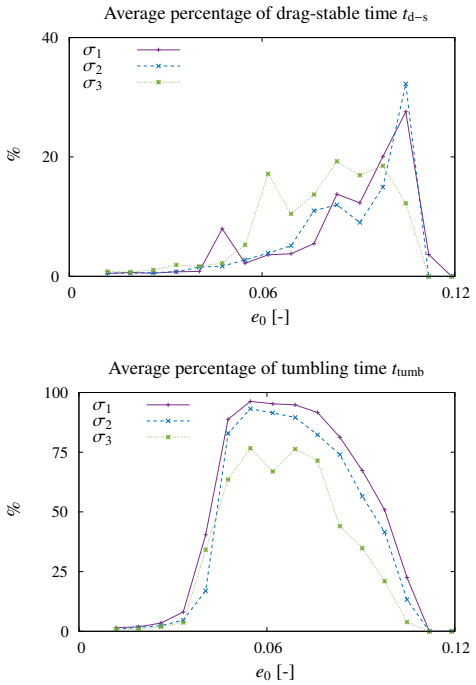

Figure 9: Average time spent in: top, drag-stable oscillations; and bottom, in a tumbling state with respect to both sunlight and the velocity vector, as a function of the initial eccentricity of the orbit, e_0. In purple (solid line), blue (dashed line) and green (dotted line) the results for σ_1, σ_2 and σ_3 are displayed, respectively.

of the decrease of all observables, as for such short integration time one cannot decide whether the motion is close to one direction or the other. For most of the e_0, the drag-stable time ranges 5%-10% of the flight time, but the rest of the motion is tumbling around the two directions of interest.

5. Discussion and future work

An analogue of the quasi-rhombic-pyramid sail [7] adapted to planar motion has been put to the test in the context of deorbiting. The attitude equations of rotation can be made explicit and dependent on physical parameters such as the aperture angle and the center of mass - center of pressure offset. This allows to study stability properties of the structures under consideration separately in SRP dominated regions and in atmospheric drag dominated regions, and to provide explicit criteria for the stability of the sun-pointing direction and relative velocity vector that depend solely on the physical parameters of the spacecraft [13].

Close to the stable orientations, the oscillatory motion can be related to previously studied models [12] used in contributions dealing with SRP acceleration for

perfectly controlled spacecraft, that reduce the phase space to a Hamiltonian one degree of freedom system [17, 19, 1, 2, 3]. These models allow to justify that one can find phase space regions where deorbiting is not due to SRP but to atmospheric drag effects, so these are transition regions where both effects play a leading role.

A discretisation of a subset of the phase space, that is in turn defined using the results of previous studies on attitude and orbit coupling [13], that only takes into account the two variables of the one degree of freedom system (instead of all 4 phase variables) is justified as enough to explain the main features of deorbiting times and auto-stabilisation either towards sunlight or the relative velocity vector. These are the initial conditions for the motion and rotation of spacecraft with different area-to-mass ratio, with minimal gravity gradient effect, to study deorbiting times essentially as a function of the initial eccentricity and the initial argument of the perigee of the osculating orbit.

The novel results derived from the presented numerical study concern auto-stabilisation of the structures under consideration. All initial orbits considered reached the minimum $r = R_\oplus + 120$ km, the faster ones being those with larger eccentricity. The maximal value of the eccentricity considered has been chosen as the critical value for passively deorbiting a spacecraft [1, 2]. All studied orbits can be characterised as follows: the deorbit time, that is, the time to reach $r = R_\oplus + 120$ km, t_{deor} can be separated in three different intervals according to the rotational dynamics around sunlight direction and the relative velocity vector, namely, there are two instants of time $t_{\text{h-s}}$ and $t_{\text{d-s}}$ such that

$$0 \leq t_{\text{h-s}} \leq t_{\text{d-s}} \leq t_{\text{deor}},$$

where, if the motion starts close enough to the sun-pointing attitude, the oscillatory character is maintained for $0 < t < t_{\text{h-s}}$ (helio-stable time), then it tumbles (librates) with respect to both sunlight and velocity vector in $t_{\text{h-s}} < t < t_{\text{d-s}}$ (drag-stable time), and finally it auto-stabilises with respect to the velocity vector due to atmospheric drag until the end of the considered motion, $t_{\text{d-s}} < t < t_{\text{deor}}$. This shows the possibilities of the kind of structures under consideration for passive deorbiting purposes.

The main future line of research that emerge from this contribution is addressing the 3D structure as proposed in the original reference [7], already initiated in the recent papers [10, 11]: the justification and measurement of non negligible regions of stability around the sunlight and velocity directions, the dynamics of oscillatory states and the effects of coupling SRP and drag and the possibilities for passive deorbiting.

Acknowledgements

The research leading to these results has received funding from the European Research Council (ERC) under the European Unions Horizon 2020 research and innovation programme as part of project COMPASS (Grant agreement No 679086). The authors acknowledge the use of the Milkyway High Performance Computing Facility, and associated support services at the Politecnico di Milano, in the completion of this work. The use of the computing facilities of the Dynamical Systems Group of the Universitat de Barcelona (Spain) are also acknowledged. The datasets generated for this study can be found in the repository at the link www.compass.polimi.it/ publications.

References

[1] C. Colombo, C. Lücking, and C. R. McInnes. Orbital dynamics of high area-to-mass ratio spacecraft with J_2 and solar radiation pressure for novel earth observation and communication services. *Acta Astronautica*, 81:137–150, 2012. doi: 10.1016/j.actaastro.2012.07.009.

[2] C. Lücking, C. Colombo, and C. R. McInnes. A passive satellite deorbiting strategy for MEO using solar radiation pressure and the J_2 effect. *Acta Astronautica*, 77:197–206, 2012. URL `http://www.scopus.com/inward/record.url?eid=2-s2.0-84864088717{&}partnerID=40{&}md5=e57a31c5a8e5ed889e49207932d64bff`.

[3] C. Lücking, C. Colombo, and C. R. McInnes. Electrochromic Orbit Control for Smart-Dust Devices. *Journal of Guidance, Control, and Dynamics*, 35(5):1548–1558, 2012. ISSN 0731-5090. doi: 10.2514/1.55488. URL `http://arc.aiaa.org/doi/10.2514/1.55488`.

[4] C. Lücking, C. Colombo, and C. R. McInnes. Solar radiation pressure-augmented deorbiting: Passive end-of-life disposal from high-altitude orbits. *Journal of Spacecraft and Rockets*, 50, 11 2013.

[5] C. Colombo and T. de Bras de Fer. Assessment of passive and active solar sailing strategies for end of life re-entry. In *International Astronautical Congress*, number IAC-16-A6.4.4, 2016.

[6] J. A. Borja and D. Tun. Deorbit Process Using Solar Radiation Force. *Journal of Spacecraft and Rockets*, 43(3):685–687, 2006. doi: 10.2514/1.28765.

[7] M. Ceriotti, P. Harkness, and M. McRobb. Variable-geometry solar sailing: the possibilities of quasi-rhombic pyramid. In M. McDonald, editor, *Advances in Solar Sailing*. Springer, 2013. ISBN 978-3-642-34906-5.

[8] M. Ceriotti, P. Harkness, and M. McRobb. Synchronized orbits and oscillations for free altitude control. *Journal of Guidance, Control, and Dynamics*, 37(6):2062–2066, 2014.

[9] M. J. Heiligers and M. Ceriotti. Orbital dynamics of an oscillating sail in the earth-moon system. In *The Fourth International Symposium on Solar Sailing 2017 17th - 20th January, 2017, Kyoto, Japan*, pages 1–10, 2017.

[10] L. Felicetti, M. Ceriotti, and P. Harkness. Attitude Stability and Altitude Control of a Variable-Geometry Earth-Orbiting Solar Sail. *Journal of Guidance, Control, and Dynamics*, 39(9):2112 – 2126, 2016.

[11] L. Felicetti, P. Harkness, and M. Ceriotti. Attitude and orbital dynamics of a variable-geometry, spinning solar sail in Earth

orbit. In *The Fourth International Symposium on Solar Sailing 2017 17th - 20th January, 2017, Kyoto, Japan*, pages 1–10, 2017.

[12] N. Miguel and C. Colombo. Attitude and orbit coupling of planar helio-stable solar sails. *arXiv e-prints*, art. arXiv:1904.00436, Mar 2019.

[13] N. Miguel and C. Colombo. Planar orbit and attitude dynamics of an Earth-orbiting solar sail under J_2 and atmospheric drag effects. *Advances in the Astronautical Sciences*, 167:299–319, 2018. Revised version available at arXiv, art.

[14] F.L. Markley and J.L. Crassidis. *Fundamentals of Spacecraft Attitude Determination and Control*. Space Technology Library. Springer New York, 2014.

[15] D.A. Vallado and W.D. McClain. *Fundamentals of Astrodynamics and Applications*. Space Technology Library. Microcosm Press, USA, fourth edition, 2013.

[16] N. Miguel, C. Simó, and A. Vieiro. From the Hénon conservative map to the Chirikov standard map for large parameter values. *Regular and Chaotic Dynamics*, 18 (5):469–489, 2013. ISSN 1560-3547. doi: 10.1134/S1560354713050018. URL `http://link.springer.com/10.1134/S1560354713050018`.

[17] W. M. Kaula. Development of the lunar and solar disturbing functions for a close satellite. *Astronomical Journal*, 67:300, June 1962. doi: 10.1086/108729.

[18] D. P. Hamilton and A. V. Krivov. Circumplanetary dust dynamics: Effects of solar gravity, radiation pressure, planetary oblateness, and electromagnetism. *Icarus*, 123(2):503–523, 1996. ISSN 00191035. doi: 10.1006/icar.1996.0175.

[19] A. V. Krivov and J. Getino. Orbital evolution of high-altitude balloon satellites. *Astron. Astrophys*, 318:308–314, 1997. ISSN 00046361.

[20] E. M. Alessi, C. Colombo, and A. Rossi. Phase space description of the dynamics due to the coupled effect of the planetary oblateness and the solar radiation pressure perturbations. *arXiv e-prints*, art. arXiv:1903.09640, Mar 2019.